


Hybrid neutron stars with the Thomas-Fermi approximation and nonlocal Nambu–Jona-Lasinio model

J. Ranjbar and M. Ghazanfari Mojarrad *

Department of Physics, Faculty of Science, University of Kashan, P.O. Box 87317-53153, Kashan, Iran

 (Received 30 April 2021; revised 18 August 2021; accepted 8 October 2021; published 22 October 2021; corrected 17 November 2021)

We probe the outcomes of the baryon-quark phase transition in the hybrid neutron star (HNS) structure with the help of the Gibbs and Maxwell constructions, adopting a semiclassical mean-field (MF) model for the equation of state (EOS) of baryonic matter based on the Thomas-Fermi (TF) approximation and a nonlocal extension of the Nambu–Jona-Lasinio (NJL) model for the EOS of the deconfined quark phase. We find that the repulsive vector contribution of the nonlocal NJL (NNJL) EOS plays an inevitable role in modeling a stable $2M_{\odot}$ HNS. Our results exclude the emergence of the pure quark phase in the inner core of a stable HNS. Within the Gibbs construction, as the quark vector interaction becomes stronger, the contribution of the baryon-quark coexisting phase in the total HNS mass is reduced. On the other hand, a stable HNS is not predicted within the Maxwell construction because it does not include a pure quark core. A comparison is made to the corresponding results employing the local (standard) NJL (LNJL) model of quark matter. Fulfilling the observational constraints, our model indicates that a neutron star (NS) with canonical mass of around $1.4M_{\odot}$ is not massive enough to be described as an HNS.

DOI: [10.1103/PhysRevC.104.045807](https://doi.org/10.1103/PhysRevC.104.045807)

I. INTRODUCTION

Neutron stars (NSs), which are generally regarded as extremely compact objects, might be constituted with a core compressed to densities exceeding several times the nuclear matter saturation density $\rho_0 \approx 0.16 \text{ fm}^{-3}$ [1]. Therefore, the dense matter composing the interior of NSs could undergo a baryon-quark phase transition among different exotic phases, creating hybrid NSs (HNSs). The equation of state (EOS) of dense matter that uses the deconfined quark phase to describe the core region of HNSs has been investigated by many authors during the past few decades [2–13]. Terrestrial evidence supporting the appearance of quark degrees of freedom in superdense matter can be found in relativistic heavy-ion collisions [14,15]. The Nambu–Jona-Lasinio (NJL) model, which can successfully reproduce many aspects of quantum chromodynamics (QCD) such as nonperturbative vacuum structure and dynamical breaking of chiral symmetry [16,17], has been one of the most efficient models for probing the EOS of quark matter and therefore the structure of HNSs. Nonlocality arising from deep analysis of low-energy quark dynamics has been suggested as an alternative approach for simulating confinement to improve the standard NJL model (which is nonconfining [18]) in both nonperturbative and perturbative regimes [19–21]. Therefore, the EOS of HNS matter using the nonlocal NJL (NNJL) model can be challenged to fulfill the stringent constraints placed by the observation of $2M_{\odot}$ pulsars [22–25], the GW170817 event [26–28], as well as

the in-progress NASA Neutron Star Interior Composition Explorer (NICER) mission [29,30]. In this work, we study the HNS structure within the Gibbs and Maxwell constructions, using the Thomas-Fermi (TF) approximation to describe the baryonic EOS [31,32] and the SU(3) version of the NNJL model [33–37] to analyze the three-flavor deconfined quark phase. The TF approximation, which was first introduced in atomic physics [38] as a semiclassical mean-field (MF) approach, can be used in a density functional based model (phenomenological model) to satisfy the nuclear physics constraints on the saturation properties of nuclear matter and finite nuclei [39,40]. Such baryonic EOSs have been successfully used to investigate the thermodynamic properties of nuclear matter [41–43] and the structure of compact objects [31,32,44–47]. Based on the considerations mentioned above, the paper is organized as follows. In Sec. II, we present the formalism for the EOS of HNS matter using the TF approximation for baryonic matter and the NNJL model for quark matter to describe the phase equilibrium between baryons and quarks via the Gibbs and Maxwell constructions. In this section, we also provide a discussion of recovering the local (standard) NJL (LNJL) model from the nonlocal Lagrangian. Section III is devoted to the investigation into the properties of HNS matter. Finally, the summary and conclusion are given in Sec. IV.

II. FORMALISM

In this section, we introduce our approach for studying the baryon-quark phase transition based on the baryonic model of TF approximation and the quark model of NNJL.

*Corresponding author: ghazanfari@kashanu.ac.ir

A. Baryonic model

The baryonic EOS is obtained by the TF approximation based on a statistical approach, using a semiclassical MF model where the state of each nucleon is specified by its momentum and position in phase space. This approximation is valid when the MF potential has a smooth behavior [38,48]. Adopting the TF approximation, we use the Myers and Swiatecki (MS) interactions of TF[90] [39] and TF[96] [40] as the Yukawa-type nucleon-nucleon interactions in phase space to present the EOS of baryonic matter, assuming that nucleons are in β equilibrium with relativistic electrons and muons:

$$V_{12} = -2 T_b \rho_0^{-1} f\left(\frac{r_{12}}{a}\right) \left\{ \frac{1}{2}(1 \mp \xi)\alpha - \frac{1}{2}(1 \mp \zeta) \left[\beta \left(\frac{p_{12}}{p_b}\right)^2 - \gamma \left(\frac{p_b}{|p_{12}|}\right) + \sigma \left(\frac{2\bar{\rho}}{\rho_0}\right)^{\frac{2}{3}} \right] \right\}, \quad (1)$$

where

$$f\left(\frac{r_{12}}{a}\right) = \frac{1}{4\pi a^3} \frac{\exp\left(-\frac{r_{12}}{a}\right)}{\frac{r_{12}}{a}}, \quad \bar{\rho}^{\frac{2}{3}} = \frac{1}{2} \left(\rho_1^{\frac{2}{3}} + \rho_2^{\frac{2}{3}} \right). \quad (2)$$

The seven adjustable parameters ($a, \xi, \zeta, \alpha, \beta, \gamma, \sigma$) in TF[90] (TF[96]) are fixed to reproduce the saturation properties of normal nuclear matter and the coefficients of the Weizsacher-Bethe semiempirical mass formula [39] ([40]):

$$\begin{aligned} a &= 0.59542 \text{ (0.59294) fm}, & \alpha &= 3.60928 \text{ (1.94684)}, \\ \beta &= 0.37597 \text{ (0.15311)}, & \gamma &= 0.21329 \text{ (1.13672)}, \\ \sigma &= 1.33677 \text{ (1.05)}, & \xi &= 0.44003 \text{ (0.27976)}, \\ \zeta &= 0.59778 \text{ (0.55665)}. \end{aligned} \quad (3)$$

For each pair of nucleons in phase space, $r_{12} = |\vec{r}_1 - \vec{r}_2|$ and $p_{12} = |\vec{p}_1 - \vec{p}_2|$ are the separation distance and relative momentum, respectively. The mean density $\bar{\rho}$ is also introduced as a function of ρ_1 and ρ_2 , being the densities of each pair of nucleons at the positions \vec{r}_1 and \vec{r}_2 , respectively. Thus, the strength of these Yukawa-type interactions depends explicitly on the momentum and density. By adopting the nuclear matter radius $r_0 = 1.13$ (1.14) for TF[90] (TF[96]), the Fermi momentum $p_b = \hbar(\frac{3}{2}\pi^2\rho_0)^{\frac{1}{3}}$ corresponding to the saturation density $\rho_0 = (\frac{4}{3}\pi r_0^3)^{-1}$, together with the associated kinetic energy $T_b = \frac{p_b^2}{2\bar{m}} = 37.679$ (37.021) where $\bar{m} = 938.903$ MeV/ c^2 is the average nucleonic mass, are incorporated into these interactions. The interactions can be distinguished with the upper signs for the like particles and the lower signs for the unlike particles. Choosing $\xi \neq \zeta$ gives a better description of the nuclear systems with higher isospin asymmetry. On the other hand, the nuclear saturation mechanism can be exploited through the competition between the attractive terms having α and γ coefficients and the repulsive terms having β and σ coefficients.

Within this statistical approach, the energy density of nuclear matter is given by

$$e_{TF} = \frac{2}{h^3} \sum_{b=n,p} \int d^3 p_1 \left[m_b c^2 + \frac{p_1^2}{2m_b} + \frac{1}{2} V_b(p_1) \right] \times \Theta(p_{F,b} - p_1), \quad (4)$$

where $V_b(p_1)$ is the MF potential of the b th nucleon, which can be expressed in terms of the Fermi momentum $p_{F,b} = (\frac{3h^3\rho_b}{8\pi})^{\frac{1}{3}}$ (corresponding to the density ρ_b):

$$V_b(p_1) = V_b^b(p_1) + \sum_{b' \neq b} V_b^{b'}(p_1), \quad (5)$$

where

$$\begin{aligned} V_b^b(p_1) &= -\frac{4T_b}{\rho_0 h^3} \left\{ \int_0^{p_{F,b}} d^3 p_2 \left[\alpha_l - \beta_l \left(\frac{p_{12}}{p_b}\right)^2 + \gamma_l \frac{p_b}{|p_{12}|} - \sigma_l \left(\frac{2\bar{\rho}}{\rho_0}\right)^{\frac{2}{3}} \right] \right\}, \\ V_b^{b'}(p_1) &= -\frac{4T_b}{\rho_0 h^3} \left\{ \sum_{b' \neq b} \int_0^{p_{F,b'}} d^3 p_2 \left[\alpha_u - \beta_u \left(\frac{p_{12}}{p_b}\right)^2 + \gamma_u \frac{p_b}{|p_{12}|} - \sigma_u \left(\frac{2\bar{\rho}}{\rho_0}\right)^{\frac{2}{3}} \right] \right\}. \end{aligned} \quad (6)$$

The interaction between the like and unlike particles can be distinguished by l and u indices indicating the minus and plus signs, respectively:

$$\begin{aligned} \alpha_{l,u} &= \frac{1}{2}(1 \mp \xi)\alpha, & \beta_{l,u} &= \frac{1}{2}(1 \mp \zeta)\beta, \\ \gamma_{l,u} &= \frac{1}{2}(1 \mp \zeta)\gamma, & \sigma_{l,u} &= \frac{1}{2}(1 \mp \zeta)\sigma. \end{aligned} \quad (7)$$

Consequently, the energy density can be expressed in terms of the Fermi momentum $p_{F,b}$ and the associated kinetic energy density $\kappa_b = \frac{8\pi p_b^2 p_{F,b}^5}{h^5}$:

$$\begin{aligned} e_{TF} &= \sum_{b,(b' \neq b)} \frac{2T_b}{\rho_0} \left\{ \frac{\rho_0 \kappa_b}{2} - \frac{\alpha_l \rho_b^2}{2} + \beta_l \rho_b \kappa_b - \frac{64\pi^2 p_b \gamma_l p_{F,b}^5}{15h^6} + \frac{\sigma_l \rho_0}{4} \left[\left(\frac{2\rho_b}{\rho_0}\right)^{\frac{5}{3}} \rho_b \right] \right\} \\ &+ \frac{2T_b}{\rho_0} \left\{ -\frac{\alpha_u \rho_b \rho_{b'}}{2} + \beta_u \rho_b \kappa_{b'} - \frac{16\pi^2 p_b \gamma_u}{h^6} \left[\left(\frac{p_{F,<}^2}{3} - \frac{p_{F,<}^5}{15}\right) \right] \right. \\ &\left. + \frac{\sigma_u \rho_0}{4} \left[\left(\frac{2\rho_b}{\rho_0}\right)^{\frac{5}{3}} \rho_{b'} \right] \right\}. \end{aligned} \quad (8)$$

Here, one can define the asymmetry parameter $\delta = \frac{\rho_n - \rho_p}{\rho_B}$, describing symmetric nuclear matter (SNM) with $\delta = 0$ and pure neutron matter (PNM) with $\delta = 1$. For β -stable nuclear matter, the β -equilibrium conditions are imposed using the chemical potential of nucleons and leptons, according to the second law of thermodynamics:

$$\mu_{e^-} = \mu_{n^0} - \mu_{p^+}, \quad (9)$$

$$\mu_{e^-} = \mu_{\mu^-}. \quad (10)$$

The chemical potential of the b th nucleon can be written as

$$\mu_b = \frac{\partial e_{TF}}{\partial \rho_b} = m_b c^2 + \frac{p_{F,b}^2}{2m_b} + \mu_b^{(l)} + \mu_b^{(u)}, \quad (11)$$

where

$$\begin{aligned} \mu_b^{(l)} &= \frac{2T_b}{\rho_0} \left\{ -\alpha_l \rho_b + \beta_l \rho_b \left(\frac{p_{F,b}}{\rho_b} \right)^2 + \beta_l \kappa_b + \sigma_l \left(\frac{2Q_b}{\rho_0} \right)^{\frac{2}{3}} \rho_b - \gamma_l \left(\frac{8\pi p_b}{h^3} \right) \left(\frac{p_{F,b}^2}{3} \right) \right\}, \\ \mu_b^{(u)} &= \sum_{b' \neq b} \frac{2T_b}{\rho_0} \left\{ -\alpha_u \rho_{b'} + \beta_u \rho_{b'} \left(\frac{p_{F,b'}}{\rho_b} \right)^2 + \beta_u \kappa_{b'} + \sigma_u \left(\frac{2Q_b}{\rho_0} \right)^{\frac{2}{3}} \left(\frac{5\rho_{b'}}{6} \right) + \sigma_u \left(\frac{2Q_{b'}}{\rho_0} \right)^{\frac{2}{3}} \left(\frac{\rho_{b'}}{2} \right) \right. \\ &\quad \left. - \gamma_u \left(\frac{8\pi p_b}{h^3} \right) \left[\left(\frac{p_{F,b'}}{3\rho_{b'}} \right) \text{ for } p_{F,b} \geq p_{F,b'} \text{ or } \left(\frac{p_{F,b}^2}{2} - \frac{p_{F,b}^2}{6} \text{ for } p_{F,b} \geq p_{F,b'} \right) \right] \right\}. \end{aligned} \quad (12)$$

In addition, the chemical potential of each lepton can be obtained by its Fermi energy:

$$\mu_{l=e^-, \mu^-} = \sqrt{(p_{F,l} c)^2 + (m_l c^2)^2}, \quad p_{F,l} = \left(\frac{3h^3 \rho_l}{8\pi} \right)^{\frac{1}{3}}. \quad (13)$$

Adding the leptonic energy density, we can determine the baryonic energy density to reach the baryonic EOS:

$$e_B = e_{TF} + e_L, \quad (14)$$

where

$$e_L = \frac{2}{h^3} \sum_{l=e^-, \mu^-} \int_0^{p_{F,l}} d^3 p \sqrt{(pc)^2 + (m_l c^2)^2}. \quad (15)$$

Consequently, imposing the charge neutrality condition $y_{p^+} = y_{e^-} + y_{\mu^-}$ (where $y_k = \frac{\rho_k}{\rho_B}$ is the relative fraction of the k th nucleon or lepton), we can obtain the pressure of baryonic matter in the β equilibrium:

$$P_B = P_{TF} + P_L = \sum_{k=b,l} (\mu_k \rho_k) - e_B. \quad (16)$$

B. Quark model

For studying the EOS of quark matter, a three-flavor version of the NNJL model is adopted using the following QCD Lagrangian in Euclidean space [34,35,49]:

$$\begin{aligned} \mathcal{L}_{QNL} &= \bar{q}(-\mathbf{i}\not{\partial} + \hat{m})q - \frac{G_S}{2} \sum_{a=0}^8 [j_a^{(S)} j_a^{(S)} + j_a^{(P)} j_a^{(P)}] \\ &\quad - \frac{G_P}{4} \sum_{a,b,c=0}^8 H_{a,b,c} [j_a^{(S)} j_b^{(S)} j_c^{(S)} - 3j_a^{(S)} j_b^{(P)} j_c^{(P)}] + \frac{G_V}{2} \sum_{a=0}^8 \sum_{\mu=1}^4 [j_a^{(V)\mu} j_a^{(V)\mu}], \end{aligned} \quad (17)$$

where q signifies a quark field including the contributions of three active flavors ($N_f = 3$) and three colors ($N_c = 3$). In this Euclidean picture, the operator $\not{\partial}$ is defined in terms of Dirac matrices γ^μ as $\not{\partial} = \gamma^\mu \partial_\mu = \vec{\gamma} \cdot \vec{\nabla} + \gamma^4 \frac{\partial}{\partial x^4}$ with $\gamma^4 = \mathbf{i}\gamma^0$ and the imaginary time variable $x^4 = it$, expressed together with the current quark mass matrix $\hat{m} = \text{diag}(m_u, m_d, m_s)$. The nonlocal nature of the interaction arises from the scalar, pseudoscalar, and vector current densities $j_a^{(S)}$, $j_a^{(P)}$, and $j_a^{(V)\mu}$, respectively, which can be written as

$$j_a^{(S)} = \int d^4 z \tilde{\mathfrak{H}}(z) \bar{q}\left(x + \frac{z}{2}\right) \lambda_a q\left(x - \frac{z}{2}\right), \quad (18)$$

$$j_a^{(P)} = \int d^4 z \tilde{\mathfrak{H}}(z) \bar{q}\left(x + \frac{z}{2}\right) \mathbf{i} \lambda_a \gamma^5 q\left(x - \frac{z}{2}\right), \quad (19)$$

$$j_a^{(V)\mu} = \int d^4 z \tilde{\mathfrak{H}}(z) \bar{q}\left(x + \frac{z}{2}\right) \lambda_a \gamma^\mu q\left(x - \frac{z}{2}\right). \quad (20)$$

where the function $\tilde{\mathfrak{H}}(z)$ is included as a form factor and λ_a with $a = 1, 2, \dots, 8$ correspond to the well-known Gell-Mann matrices in the color space together with $\lambda_0 = \sqrt{2/3} \mathbb{1}_{3 \times 3}$. In the model, the scalar and pseudoscalar four-quark interaction

with the coupling G_S , the Kobayashi-Maskawa-'t Hooft six-quark interaction with the coupling G_p accompanied by $H_{a,b,c} = \frac{1}{3!} \epsilon_{ijk} \epsilon_{mnl} (\lambda_a)_{im} (\lambda_b)_{jn} (\lambda_c)_{kl}$, and the vector four-quark interaction with the coupling G_V are taken into account.

Within the MF approximation, the zero-temperature grand canonical thermodynamic potential [35–37] can be introduced as

$$\begin{aligned} \Omega_{QNL} = & - \sum_{i=u,d,s} \overbrace{\frac{3}{\pi^3} \int_0^\infty dp_0 \int_0^\infty dp p^2}^{\frac{2N_c}{(2\pi)^4} \int d^4p} \ln \left(\frac{\widehat{\omega}_i^2 + M_i^2(\omega_i^2)}{\omega_i^2 + m_i^2} \right) - \sum_{i=u,d,s} \frac{3}{\pi^2} \int_0^{\sqrt{\mu_i^2 - m_i^2}} dp p^2 (\mu_i - \sqrt{p^2 + m_i^2}) \Theta(\mu_i - m_i) \\ & - \sum_{i=u,d,s} \frac{1}{2} (\bar{\sigma}_i \bar{S}_i + \frac{G_S}{2} \bar{S}_i^2) - \frac{G_p}{4} (\bar{S}_u \bar{S}_d \bar{S}_s) - \sum_{i=u,d,s} \frac{\bar{V}_i^2}{4G_V}, \end{aligned} \quad (21)$$

where the momentum-dependent constituent quark mass $M_i(\omega_i^2) = m_i + \mathfrak{R}(\omega_i^2) \bar{\sigma}_i$ and the squared four-momentum $\omega_i^2 = (p_0 + \mathbf{i} \mu_i)^2 + p^2$ are introduced using m_i , μ_i , and $\bar{\sigma}_i$ as the current mass, chemical potential and scalar MF of the i th quark flavor, respectively. The auxiliary MF \bar{S}_i is related to the scalar MF $\bar{\sigma}_i$ within the stationary phase approximation. The Fourier transform of the form factor $\mathfrak{R}(z)$ in Euclidean space turns out to be the Gaussian function $\mathfrak{R}(\omega_i^2) = \exp(-\omega_i^2/\hat{\Lambda}^2)$, which is used to regulate the nonlocal interactions. The vector MF \bar{V}_i shifts the chemical potential μ_i [21], rendering the dressed part of the thermodynamic potential as follows:

$$\mu_i \rightarrow \widehat{\mu}_i = \mu_i - \mathfrak{R}(\omega_i^2) \bar{V}_i, \quad (22)$$

$$\omega_i^2 \rightarrow \widehat{\omega}_i^2 = (p_0 + \mathbf{i} \widehat{\mu}_i)^2 + p^2. \quad (23)$$

Besides the model parameter $\hat{\Lambda}$ being related to the stiffness of the chiral transition, the current mass of each quark flavor m_i and the coupling constants G_S , G_p are fixed to

reproduce the pion decay constant f_π and the meson masses m_π , m_K , $m_{\eta'}$ [19,20]. In the present calculations, we use the nonlocal interaction set $m_s = 140.7$ (127.8) MeV (treated as a free parameter), $\hat{\Lambda} = 706.0$ (780.6) MeV, $m_u = m_d = 6.2$ (5.5) MeV, $G_S = \frac{15.04}{\hat{\Lambda}^2}$ ($\frac{14.48}{\hat{\Lambda}^2}$), $G_p = -\frac{337.71}{\hat{\Lambda}^5}$ ($\frac{267.24}{\hat{\Lambda}^5}$) from Refs. [34,35] ([9,37]), labeled as NNJL I (II). Due to the uncertainty in the theoretical predictions of the vector coupling constant G_V , we introduce the vector strength ratio $\eta_V = G_V/G_S$ as a free parameter [50].

For a mixture of quarks and leptons, the β -equilibrium conditions can be written in terms of the baryonic chemical potential $\mu_B = \frac{2\mu_d + \mu_u}{3}$ and the electron chemical potential μ_e :

$$\begin{aligned} \mu_{u^+} &= \mu_B - \frac{2\mu_e}{3}, & \mu_{d^-} &= \mu_{s^-} = \mu_B + \frac{\mu_e}{3}, \\ \mu_{\mu^-} &= \mu_e. \end{aligned} \quad (24)$$

Imposing the β -equilibrium conditions, one can obtain the MF values $\bar{\sigma}_i$, \bar{S}_i , \bar{V}_i by minimizing the thermodynamic potential Ω_{QNL} as follows:

$$\frac{\partial \Omega_{QNL}}{\partial \bar{\sigma}_i} = 0 \Rightarrow \bar{S}_i = - \overbrace{\frac{12}{\pi^3} \int_0^\infty dp_0 \int_0^\infty dp p^2}^{\frac{8N_c}{(2\pi)^4} \int d^4p} \mathfrak{R}(\omega_i^2) \frac{M_i(\omega_i^2)}{\widehat{\omega}_i^2 + M_i^2(\omega_i^2)}, \quad (25)$$

$$\frac{\partial \Omega_{QNL}}{\partial \bar{S}_i} = 0 \Rightarrow \bar{\sigma}_i = -G_S \bar{S}_i - \frac{G_p}{2} \bar{S}_j \bar{S}_k, \quad (26)$$

$$\frac{\partial \Omega_{QNL}}{\partial \bar{V}_i} = 0 \Rightarrow \bar{V}_i = - \overbrace{\frac{12G_V}{\pi^3} \int_0^\infty dp_0 \int_0^\infty dp p^2}^{\frac{8N_c G_V}{(2\pi)^4} \int d^4p} \mathfrak{R}(\omega_i^2) \frac{\widehat{\mu}_i - \mathbf{i} p_0}{\widehat{\omega}_i^2 + M_i^2(\omega_i^2)}. \quad (27)$$

In the so-called gap equation (26), (i, j, k) indicate any permutation of (u, d, s) quarks. For a neutral mixture of quarks and leptons in the β equilibrium, μ_B is employed as an input to solve the coupled equations self-consistently so that μ_e can be fixed using the following charge neutrality condition:

$$\frac{2}{3} \rho_{u^+} - \frac{1}{3} (\rho_{d^-} + \rho_{s^-}) - (\rho_{e^-} + \rho_{\mu^-}) = 0, \quad (28)$$

where the number density of the i th quark flavor is calculated by $\rho_i = -\frac{\partial \Omega_{QNL}}{\partial \mu_i}$. Here, we can also introduce the relative quark fraction $y_{(i=u,d,s)} = \frac{\rho_i}{3\rho_B}$ at a given baryonic density

$\rho_B = (\rho_u + \rho_d + \rho_s)/3$. Finally, the pressure P_Q and energy density e_Q for the EOS of quark matter are given by

$$P_Q = P_{QNL} + P_L, \quad (29)$$

$$e_Q = \sum_{k=u^+, d^-, s^-, e^-, \mu^-} \rho_k \mu_k - P_Q. \quad (30)$$

In the above relation, we adopt $P_{QNL} = \Omega_{QNL}^0 - \Omega_{QNL}$ using Ω_{QNL}^0 to ensure the requirement $P_{QNL} = 0$ in the vacuum.

It is worth mentioning that the standard NJL model is trivially recovered via inserting the form factor $\tilde{\eta}(z) = \delta(z)$ into the integrals of Eqs. (18)–(20). At the MF level [17], the constituent quark mass M_i and renormalized chemical potential $\tilde{\mu}_i$ are introduced as

$$M_i = m_i - 2G_S \langle \bar{q}_i q_i \rangle - 2G_p \langle \bar{q}_j q_j \rangle \langle \bar{q}_k q_k \rangle, \quad (31)$$

$$\tilde{\mu}_i = \mu_i - 2G_V \langle q_i^\dagger q_i \rangle, \quad (32)$$

$$\begin{aligned} \Omega_{QL} = & - \sum_{i=u,d,s} \frac{3}{\pi^2} \int_0^{\hat{\Lambda}} dp p^2 [E_p^{(M_i)} + (\tilde{\mu}_i - E_p^{(M_i)}) \Theta(\tilde{\mu}_i - E_p^{(M_i)})] + \sum_{i=u,d,s} G_S \langle \bar{q}_i q_i \rangle^2 \\ & + 4G_p \langle \bar{q}_u q_u \rangle \langle \bar{q}_d q_d \rangle \langle \bar{q}_s q_s \rangle - \sum_{i=u,d,s} \frac{(\tilde{\mu}_i - \mu_i)^2}{4G_V}; \quad E_p^{(M_i)} = \sqrt{p^2 + M_i^2}. \end{aligned} \quad (33)$$

Using Eqs. (31) and (32), $\langle \bar{q}_i q_i \rangle$ and $\langle q_i^\dagger q_i \rangle$ are obtained by minimizing Ω_{QL} with respect to M_i and $\tilde{\mu}_i$, respectively ($\tilde{\mu}_i \leq \hat{\Lambda}$):

$$\frac{\partial \Omega_{QL}}{\partial M_i} = 0 \Rightarrow \langle \bar{q}_i q_i \rangle = -\frac{3}{\pi^2} \int_0^{\hat{\Lambda}} dp p^2 \frac{M_i}{E_p^{(M_i)}} [1 - \Theta(\tilde{\mu}_i - E_p^{(M_i)})], \quad (34)$$

$$\frac{\partial \Omega_{QL}}{\partial \tilde{\mu}_i} = 0 \Rightarrow \langle q_i^\dagger q_i \rangle = \rho_i = +\frac{3}{\pi^2} \int_0^{\hat{\Lambda}} dp p^2 \Theta(\tilde{\mu}_i - E_p^{(M_i)}). \quad (35)$$

For comparison, we also perform the standard NJL calculations using the RKH (HK) [51] ([52]) set with $m_s = 140.7$ (135.7) MeV, $\hat{\Lambda} = 602.3$ (631.4) MeV, $m_u = m_d = 5.5$ (5.5) MeV, $G_S = \frac{3.67}{\hat{\Lambda}^2}$ ($\frac{3.67}{\hat{\Lambda}^2}$), $G_p = -\frac{12.36}{\hat{\Lambda}^5}$ ($-\frac{9.29}{\hat{\Lambda}^5}$), as $P_{QL} = \Omega_{QL}^0 - \Omega_{QL}$ is adopted to fulfill the vacuum pressure $P_{QL} = 0$.

C. Baryon-quark phase transition

In a systematic analysis of the baryon-quark mixed phase, both the Gibbs and Maxwell constructions indicate the bulk properties without including the geometrical (pasta) structures constituted by the finite-size effects like surface and Coulomb energies, describing the two limiting cases of zero and sufficiently large values of the poorly known baryon-quark surface tension, respectively. In the Gibbs construction, the following conditions hold between both phases at a given μ_B :

$$\mu_B^{(BP)} = \mu_B^{(QP)} \equiv \mu_b; \quad \mu_B^{(BP)} = \frac{\mu_n}{3}, \quad (36)$$

$$\mu_e^{(BP)} = \mu_e^{(QP)} \equiv \mu_e, \quad (37)$$

$$P^{(BP)}[\mu_b, \mu_e] = P^{(QP)}[\mu_b, \mu_e]. \quad (38)$$

Therefore, the volume fraction χ_Q ($0 \leq \chi_Q \leq 1$) occupied by quark matter in the mixed phase is obtained from the condition of global charge neutrality as follows:

$$(1 - \chi_Q) \rho_C^{(BP)} + \chi_Q \rho_C^{(QP)} = 0, \quad (39)$$

where

$$\rho_C^{(BP)} = \rho_{p^+}^{(BP)} - \rho_{e^-}^{(BP)} - \rho_{\mu^-}^{(BP)}, \quad (40)$$

$$\rho_C^{(QP)} = \frac{2}{3} \rho_{u^+}^{(QP)} - \frac{1}{3} \rho_{d^-}^{(QP)} - \frac{1}{3} \rho_{s^-}^{(QP)} - \rho_{e^-}^{(QP)} - \rho_{\mu^-}^{(QP)}. \quad (41)$$

where $\langle \bar{q}_i q_i \rangle$ is the quark condensate and $\langle q_i^\dagger q_i \rangle$ denotes the i th quark number density $\rho_i = \frac{p_{F,i}^3}{\pi^2}$ ($p_{F,i}$ being the corresponding Fermi momentum), as (i, j, k) indicate any permutation of (u, d, s) quarks. Since the standard NJL model is non-renormalizable, the regularization scheme is provided by the ultraviolet cutoff parameter $\hat{\Lambda}$ in the MF thermodynamic potential as follows:

Consequently, the baryonic density $\rho_B^{(MP)}$ and energy density $e^{(MP)}$ of the mixed phase are extracted from

$$\rho_B^{(MP)} = (1 - \chi_Q) \rho_B^{(BP)} + \chi_Q \rho_B^{(QP)}, \quad (42)$$

$$e^{(MP)} = (1 - \chi_Q) e^{(BP)} + \chi_Q e^{(QP)}. \quad (43)$$

A sharp phase transition takes place in the Maxwell construction where the phase transition conditions are imposed by $\mu_B^{(BP)} = \mu_B^{(QP)}$ and $P^{(BP)} = P^{(QP)}$, as the pure phases are independently taken to be locally charge neutral. When the charge screening effects become strong, the Maxwell scenario turns out to be favored for any surface tension being greater than a critical value $\tilde{\sigma}_c$, which [13,53] can be estimated by

$$\tilde{\sigma}_c = \frac{(\mu_e^{(BP)} - \mu_e^{(QP)})^2}{8\pi \alpha_e (\lambda_D^{(BP)} + \lambda_D^{(QP)})}, \quad (44)$$

where $\alpha_e \simeq \frac{1}{137}$ is the fine-structure constant and $\lambda_D^{(S)} = (-4\pi \alpha_e \frac{\partial \rho_C^{(S)}}{\partial \mu_e})^{-\frac{1}{2}}$ denotes the Debye screening length of the S th phase.

III. RESULTS AND DISCUSSION

Within the Gibbs and Maxwell construction, we investigate the deconfinement phase transition in HNSs, adopting the baryonic EOS of TF (TF[90] and TF[96]) and the quark EOS of NNJL (the interaction sets I and II), and paying special attention to the role of the quark repulsive vector interaction.

As a first step, it is worthwhile to basically present the nuclear matter EOS of TF at supersaturation densities. To this purpose, we show in Fig. 1 the pressure of SNM and PNM as a function of baryonic density. As clearly seen, the baryonic interaction of TF[90] gives a stiffer EOS than

TABLE I. Domain of the mixed-phase region in terms of baryonic density, energy density, baryonic chemical potential, and pressure, for the quark interactions of NNJL I and II at $\eta_v = 0, 0.04, 0.08$, combined with the baryonic interactions of TF[90] and TF[96] via the Gibbs [Maxwell] construction.

| EOS | η_v | $\rho^{(BP)}-\rho^{(QP)}$ (fm^{-3}) | $e^{(BP)}-e^{(QP)}$ (GeVfm^{-3}) | $\mu_B^{(BP)}-\mu_B^{(QP)}$ (MeV) | $p^{(BP)}-p^{(QP)}$ (MeVfm^{-3}) |
|----------------|----------|---|--|--------------------------------------|--|
| TF[90]-NNJL I | 0 | 0.60–1.39 [0.71–1.31] | 0.64–1.75 [0.79–1.63] | 428.10–481.26 [472.98] | 135.52–257.72 [224.23] |
| | 0.04 | 0.69–1.41 [0.79–1.35] | 0.76–1.84 [0.90–1.75] | 463.07–513.97 [506.20] | 203.32–331.44 [299.36] |
| | 0.08 | 0.82–1.35 [0.90–1.34] | 0.95–1.83 [1.08–1.81] | 521.21–564.92 [558.63] | 335.76–459.18 [432.79] |
| TF[96]-NNJL I | 0 | 0.68–1.54 [0.83–1.43] | 0.73–1.96 [0.93–1.80] | 435.11–495.81 [485.16] | 160.70–321.52 [274.20] |
| | 0.04 | 0.80–1.56 [0.93–1.49] | 0.89–2.08 [1.08–1.96] | 476.31–534.32 [524.77] | 252.60–422.44 [378.44] |
| | 0.08 | 0.99–1.48 [1.08–1.44] | 1.18–2.04 [1.34–1.98] | 550.68–598.70 [592.62] | 452.93–612.99 [583.46] |
| TF[90]-NNJL II | 0 | 0.62–1.36 [0.71–1.28] | 0.66–1.70 [0.79–1.59] | 435.47–480.64 [472.42] | 149.02–255.48 [223.02] |
| | 0.04 | 0.67–1.38 [0.77–1.32] | 0.73–1.79 [0.88–1.69] | 455.10–505.69 [497.93] | 187.04–311.41 [279.93] |
| | 0.08 | 0.76–1.40 [0.85–1.36] | 0.86–1.88 [0.99–1.80] | 492.26–538.93 [531.76] | 266.90–391.92 [362.21] |
| TF[96]-NNJL II | 0 | 0.69–1.51 [0.83–1.40] | 0.73–1.93 [0.93–1.77] | 435.77–495.62 [485.15] | 162.05–319.99 [274.17] |
| | 0.04 | 0.78–1.55 [0.90–1.47] | 0.86–2.05 [1.04–1.91] | 467.01–525.03 [515.26] | 230.58–396.53 [352.31] |
| | 0.08 | 0.90–1.58 [1.01–1.52] | 1.04–2.18 [1.21–2.07] | 513.69–566.48 [557.44] | 348.06–515.23 [473.16] |

the one of TF[96]. It can be concluded from this figure that the results of the TF model are compatible with the

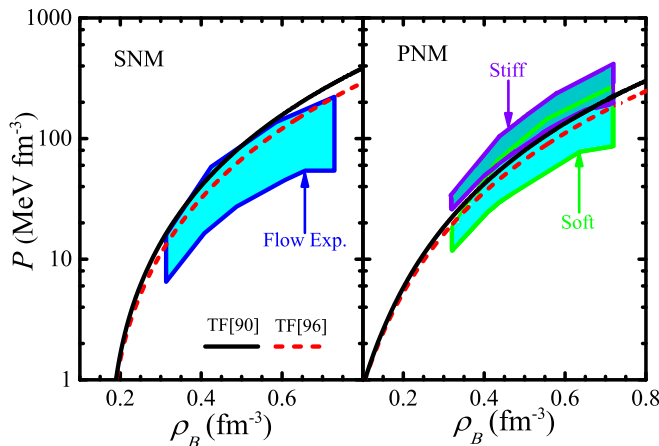


FIG. 1. Pressure of SNM (left panel) and PNM (right panel) as a function of baryonic density. The results are compared with the ones obtained from the flow data analysis of heavy-ion collisions [54].

measurements obtained from analysis of collective flows in heavy ion collision experiments [54], although the SNM EOS of TF[90] lies near the upper boundary of the flow data region.

In the plane of pressure and baryonic chemical potential, the crossing between the baryonic and quark EOSs gives rise to the emergence of the baryon-quark mixed phase (see Fig. 2). Note that in this figure the intercepts indicate a high transition pressure for all hybrid EOSs, which is more remarkable for TF[96] being joined to the larger values of the vector coupling strength η_v . In general, a more high-pressure mixed phase can be formed with NNJL I. As a starting point for describing our hybrid EOSs, Table I presents the domain of the baryon-quark mixed phase obtained by the Gibbs and Maxwell constructions in terms of the baryonic density, energy density, baryonic chemical potential, and pressure.

The baryonic chemical potential plays a fundamental role in the study of dense stellar matter. Figure 3 shows the baryonic chemical potential at various baryonic (energy) densities. As seen in the mixed-phase region using the Gibbs construction, the baryonic chemical potential increases smoothly with the baryonic (energy) density, while the mixed phase

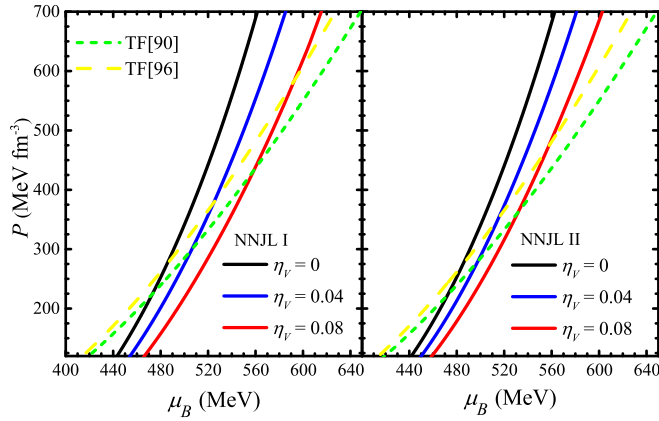


FIG. 2. Pressure as a function of baryonic chemical potential for the quark interactions of NNJL I (left panel) and NNJL II (right panel) at $\eta_v = 0, 0.04, 0.08$, together with the baryonic interactions of TF[90] (short dashes) and TF[96] (long dashes).

is described by the plateau within the Maxwell construction. However, the baryonic chemical potential grows drastically when the repulsive vector contribution in quark matter becomes stronger, as seen more considerably for NNJL I. It can be generally indicated that the mixed phases de-

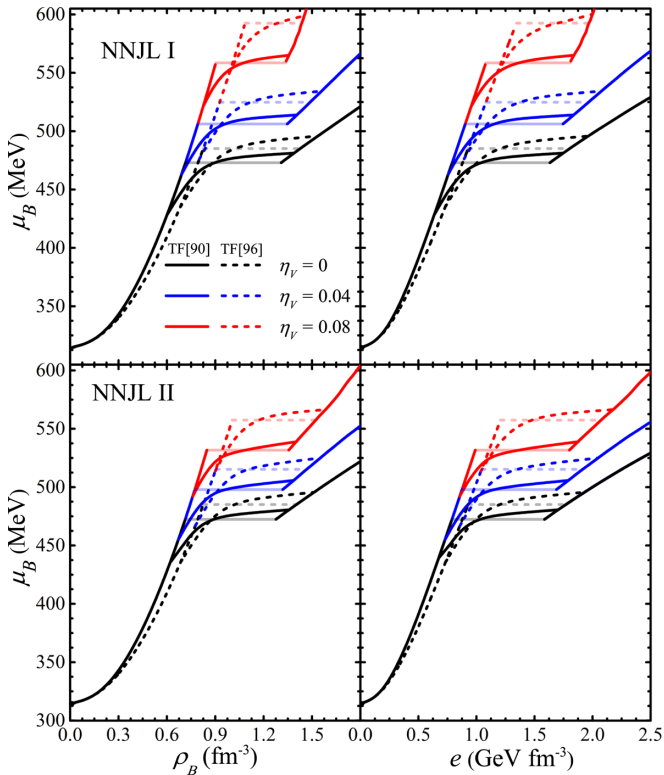


FIG. 3. Baryonic chemical potential as a function of baryonic density (left panels) and energy density (right panels) for the quark interactions of NNJL I (upper panels) and NNJL II (lower panels) at $\eta_v = 0, 0.04, 0.08$, combined with the baryonic interactions of TF[90] (solid lines) and TF[96] (dashed lines) via the Gibbs construction, as the plateaus correspond to the Maxwell construction.

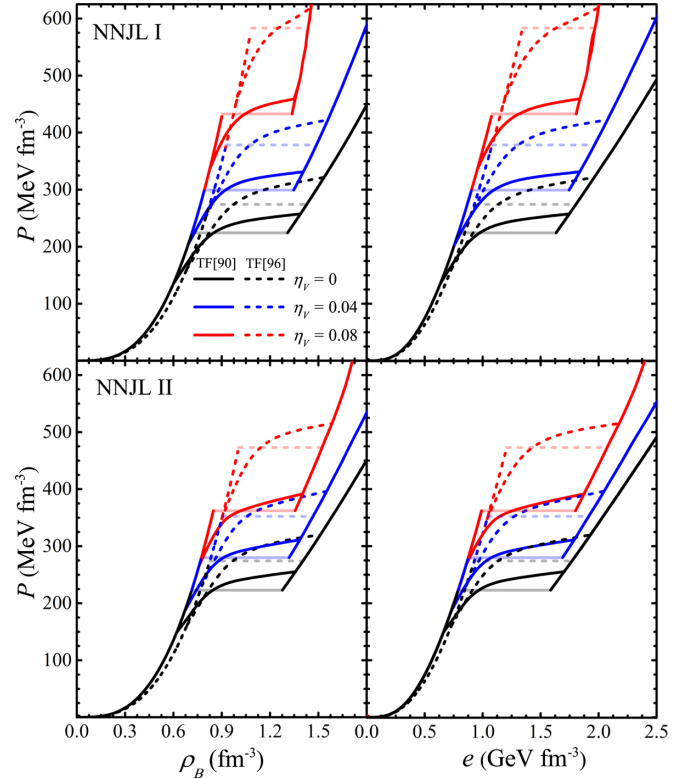


FIG. 4. Pressure as a function of baryonic density (left panels) and energy density (right panels) for the quark interactions of NNJL I (upper panels) and NNJL II (lower panels) at $\eta_v = 0, 0.04, 0.08$, combined with the baryonic interactions of TF[90] (solid lines) and TF[96] (dashed lines) via the Gibbs construction, as the plateaus correspond to the Maxwell construction.

scribed with TF[96] and NNJL I emerge with higher baryonic chemical potentials than the ones obtained with TF[90] and NNJL II.

The pressure is one of the most outstanding feature of the EOS for compact objects due to its key role in nuclear astrophysics. We show in Fig. 4 the pressure as an increasing function of baryonic (energy) density, which rises smoothly (shows the plateau) in the mixed phase under the Gibbs (Maxwell) construction (similar to the baryonic chemical potential). As expected, the region of the mixed phase for the Maxwell construction is located inside the one for the Gibbs construction. It is seen that the stiffness of hybrid EOS, especially in the quark branch, shows a significant influence on the characteristics of the mixed phase. Besides strengthening the repulsive vector interaction between quarks (increasing η_v), using the more repulsive interactions of TF[90] and NNJL I leads to a stiffer hybrid EOS. As similarly indicated in Ref. [35] for the baryonic EOSs of RMF (using the GM1 and NL3 parametrizations), the width of the mixed phase for the ones of TF becomes significantly smaller if the quark EOSs of NNJL with larger η_v are taken into account in the hybrid EOSs. In general, the more repulsive quark EOSs push the threshold formation of the mixed phase toward higher baryonic (energy) densities. For better understanding the properties of the mixed phase, the pressure versus the

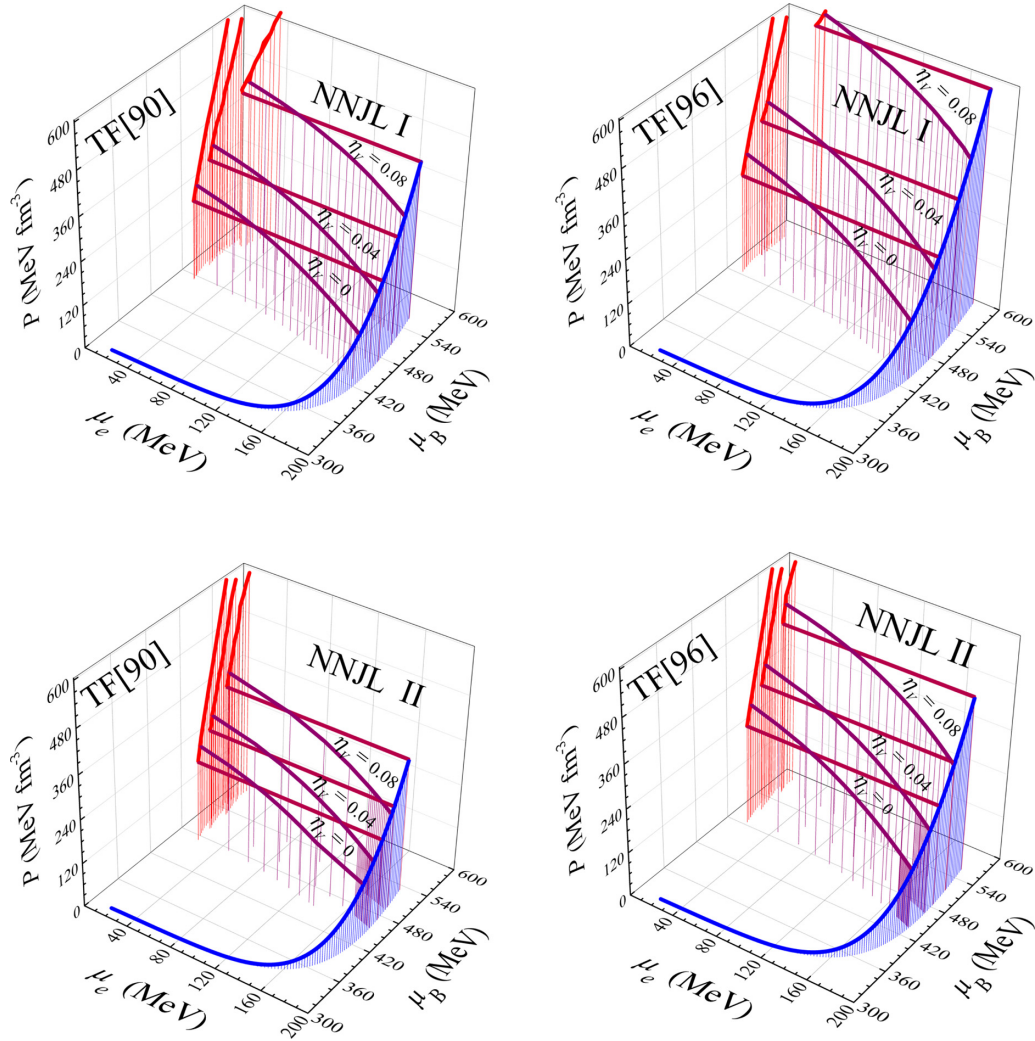


FIG. 5. Pressure as a function of baryonic and electron chemical potentials for the quark interactions of NNJL I (upper panels) and NNJL II (lower panels) at $\eta_v = 0, 0.04, 0.08$, combined with the baryonic interactions of TF[90] (left panels) and TF[96] (right panels) via the Gibbs construction, as the plateaus correspond to the Maxwell construction.

baryonic and electron chemical potentials is displayed in three-dimensional space (see Fig. 5). Contrary to the behavior of both the pressure and baryonic chemical potential in the baryon-quark coexistence phase, the electron chemical potential shows a significant drop as the system transforms to the pure quark phase. It can be generally seen that the stiffer quark EOSs shift the onset of the mixed phase to the higher values of pressure and baryonic chemical potential, while the lower ones are obtained by the stiffer baryonic EOS (TF[90]).

In order to extract the structure of HNSs, each of our hybrid EOSs provides an input for the well-known Tolman-Oppenheimer-Volkoff equations [55,56]:

$$\frac{dP(r)}{dr} = -\frac{Gm(r)e(r)}{r^2} \frac{\left[1 + \frac{P(r)}{e(r)c^2}\right] \left[1 + \frac{4\pi r^3 P(r)}{m(r)c^2}\right]}{1 - \frac{2Gm(r)}{rc^2}}, \quad (45)$$

$$\frac{dm(r)}{dr} = 4\pi r^2 e(r), \quad (46)$$

in which P , e , G and m denote the pressure, energy density, gravitational constant, and star mass within radius r , respectively. Starting from a central energy density e_c , we compute the pressure up to the one corresponding to the density of iron at the star radius R . For the HNS crust, we have joined the inner crust using the EOS of Negele and Vauthrun [57], which is based on the Hartree-Fock approach, and the outer crust using the one of Baym *et al.* [58], which relies on the properties of heavy nuclei. In Fig. 6, we show the gravitational mass $M = m(R)$ (in units of the solar mass M_\odot) as a function of the central baryonic (energy) density ρ_c (e_c). As seen in this figure, the gravitational mass reaches a maximum value, which is denoted by a circle. The EOS above the respective values of ρ_c and e_c in the maximum mass configuration (circle points) is excluded due to the star instability against radial oscillations. We also signify the deconfinement phase transition by a triangle (vertical slash) for the Gibbs (Maxwell) construction. As expected, the larger values of the maximum mass are obtained by the stiffer hybrid EOSs. For all hybrid EOSs, since the respective central baryonic

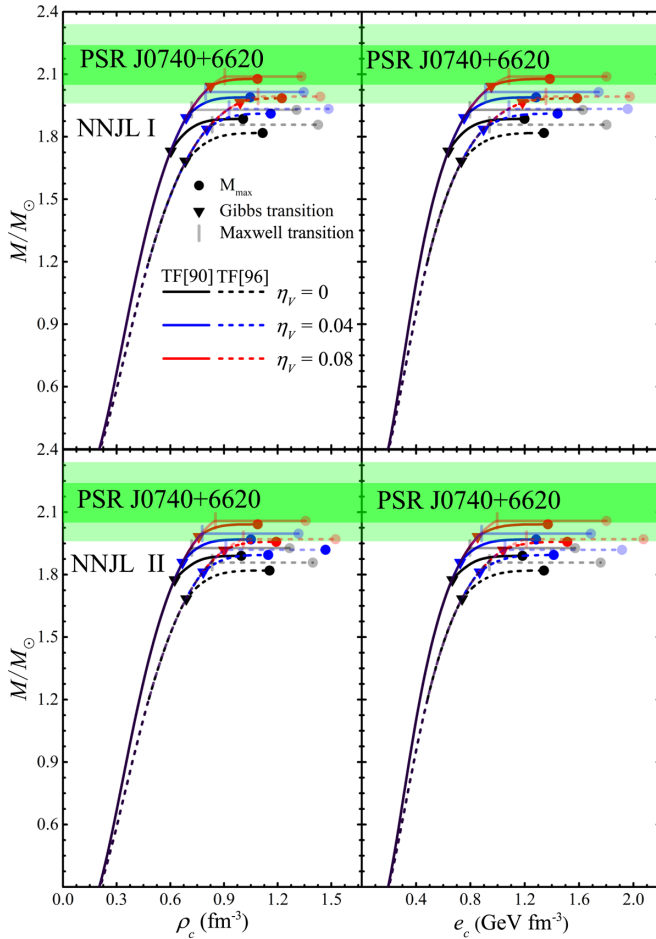


FIG. 6. Gravitational mass of HNSs (in units of the solar mass M_\odot) as a function of central baryonic density (left panels) and central energy density (right panels) for the quark interactions of NNJL I (upper panels) and NNJL II (lower panels) at $\eta_v = 0, 0.04, 0.08$, combined with the baryonic interactions of TF[90] (solid lines) and TF[96] (dashed lines) via the Gibbs and constructions, as the plateaus correspond to the Maxwell construction. The circles indicate the maximum mass configurations, as the EOS above the respective baryonic densities and energy densities is excluded. The onset of the baryon-quark phase transition in the star center is shown with the triangles and vertical slashes corresponding to the Gibbs and Maxwell constructions, respectively. The horizontal band shows the observational mass constraint from PSR J0740 + 6620 [25].

(energy) density of the maximum mass configuration sets in the mixed phase, pure quark phase cannot occur in the core of an HNS.

For each hybrid EOS described with the Gibbs construction (which predicts an HNS without a pure-quark core), the mass fraction of the baryon-quark mixed-phase core $M_{(MP)}/M$ is shown in Fig. 7. It is shown in this figure that when using a stiffer quark EOS with larger η_v , the mass fraction lies within a smaller range of values. As also realized from Table II (III) where the properties of the maximum mass configuration are summarized using the NNJL (LNJL) model, within the the Gibbs construction, $M_{(MP)}/M$ cannot exceed a value of about $\approx 19\%$ (13%), while a $2M_\odot$ HNS can be constituted

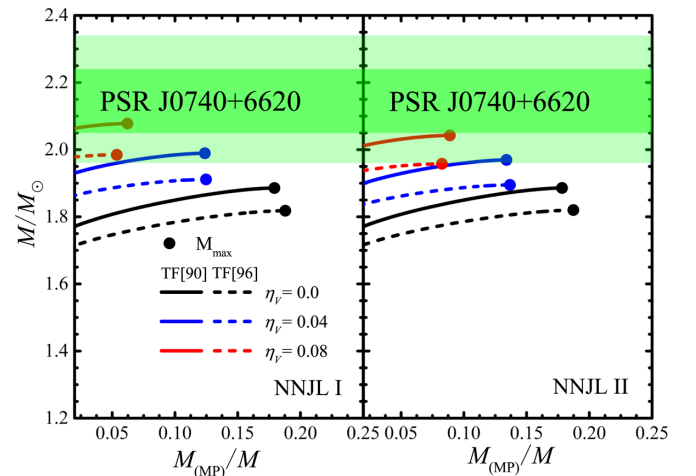


FIG. 7. Gravitational mass of HNSs (in units of the solar mass M_\odot) as a function of mixed-phase mass fraction for the quark interactions of NNJL I (left panel) and NNJL II (right panel) at $\eta_v = 0, 0.04, 0.08$, combined with the baryonic interactions of TF[90] (solid lines) and TF[96] (dashed lines) via the Gibbs construction. The circles indicate the maximum mass configurations. The horizontal band shows the observational mass constraint from PSR J0740 + 6620 [25].

with the smaller amounts of the mass fraction up to about $\approx 12\%$ (7%). On the other hand, we display in Fig. 8 the permitted values of the quark volume fraction χ_Q in the HNS structure for the hybrid EOSs based on the Gibbs construction. Evidently, χ_Q is an increasing function of ρ_B for each case of HNS matter. Furthermore, the allowed range of χ_Q is not sensitive to the case of the hybrid EOS employed in this study.

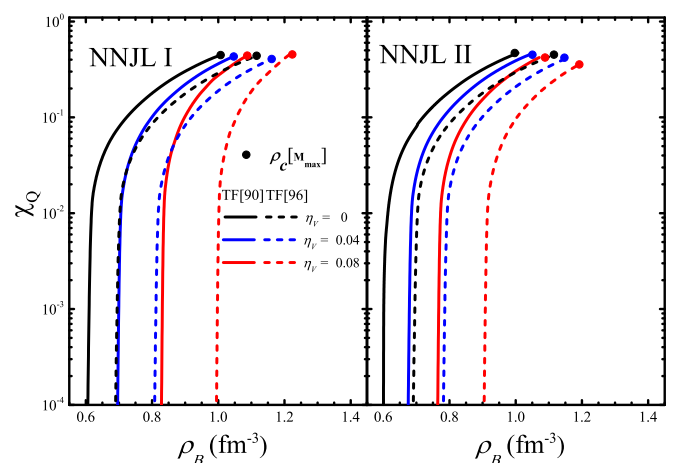


FIG. 8. Quark volume fraction as a function of baryonic density for the quark interactions of NNJL I (left panel) and NNJL II (right panel) at $\eta_v = 0, 0.04, 0.08$, combined with the baryonic interactions of TF[90] (solid lines) and TF[96] (dashed lines) via the Gibbs construction. The circles indicate the baryonic densities and quark volume fractions in the center of the respective maximum mass configurations.

TABLE II. Characteristics of the maximum mass configuration in terms of central baryonic density ρ_c , central energy density e_c , central pressure P_c , gravitational mass M_{\max} (in units of the solar mass M_\odot), star radius R , mixed-phase mass fraction $M_{(MP)}/M_{\max}$, and tidal deformability Λ for the quark interactions of NNJL I and II at $\eta_V = 0, 0.04, 0.08$, combined with the baryonic interactions of TF[90] and TF[96] via the Gibbs [Maxwell] construction ($\tilde{\sigma}_c$ being the critical surface tension).

| EOS | η_V | ρ_c (fm^{-3}) | e_c (GeVfm^{-3}) | P_c (MeVfm^{-3}) | M_{\max} (M_\odot) | R (km) | $\frac{M_{(MP)}}{M_{\max}}$ | Λ | $\tilde{\sigma}_c$ (MeVfm^{-2}) |
|----------------|----------|----------------------------------|----------------------------------|----------------------------------|-----------------------------|------------------|-----------------------------|------------------|---|
| TF[90]-NNJL I | 0 | 1.01 [0.71–1.31] | 1.20 [0.79–1.63] | 242.61 [224.23] | 1.89 [1.93] | 11.45 [11.54] | 0.18 [0] | 32.78 [30.13] | 53.98 |
| | 0.04 | 1.05 [0.79–1.35] | 1.28 [0.90–1.75] | 315.66 [299.36] | 1.99 [2.01] | 11.27 [11.31] | 0.12 [0] | 18.85 [17.87] | 51.75 |
| | 0.08 | 1.09 [0.90–1.34] | 1.38 [1.08–1.81] | 439.42 [432.79] | 2.08 [2.09] | 10.98 [10.98] | 0.06 [0] | 10.28 [9.86] | 42.65 |
| TF[96]-NNJL I | 0 | 1.12 [0.83–1.43] | 1.34 [0.93–1.80] | 295.68 [274.20] | 1.82 [1.86] | 10.92 [11.00] | 0.19 [0] | 28.03 [25.83] | 62.74 |
| | 0.04 | 1.16 [0.93–1.49] | 1.44 [1.08–1.96] | 393.60 [378.44] | 1.91 [1.93] | 10.69 [10.71] | 0.12 [0] | 15.76 [14.86] | 60.12 |
| | 0.08 | 1.22 [1.08–1.44] | 1.59 [1.34–1.98] | 577.90 [583.46] | 1.98 [1.99] | 10.32 [10.30] | 0.05 [0] | 8.19 [7.76] | 42.75 |
| TF[90]-NNJL II | 0 | 1.00 [0.71–1.28] | 1.18 [0.79–1.59] | 241.81 [223.02] | 1.89 [1.93] | 11.47 [11.54] | 0.18 [0] | 32.42 [30.44] | 50.77 |
| | 0.04 | 1.05 [0.77–1.32] | 1.28 [0.88–1.69] | 295.18 [279.93] | 1.97 [2.00] | 11.32 [11.37] | 0.13 [0] | 21.33 [20.09] | 49.50 |
| | 0.08 | 1.09 [0.85–1.36] | 1.37 [0.99–1.80] | 370.62 [362.21] | 2.04 [2.06] | 11.13 [11.14] | 0.09 [0] | 13.68 [13.01] | 46.46 |
| TF[96]-NNJL II | 0 | 1.12 [0.83–1.40] | 1.34 [0.93–1.77] | 295.40 [274.17] | 1.82 [1.86] | 10.92 [11.00] | 0.19 [0] | 27.91 [25.84] | 59.79 |
| | 0.04 | 1.15 [0.90–1.47] | 1.41 [1.04–1.91] | 369.76 [352.31] | 1.89 [1.92] | 10.74 [10.78] | 0.14 [0] | 17.74 [16.72] | 58.21 |
| | 0.08 | 1.19 [1.01–1.52] | 1.51 [1.21–2.07] | 484.15 [473.16] | 1.96 [1.97] | 10.49 [10.50] | 0.08 [0] | 10.90 [10.48] | 54.75 |

Within the Gibbs construction, using only the allowed baryonic density range of HNS matter, we display the number fraction of particles y_i in Figs. 9 and 10 using the NNJL I and II, respectively. It is seen that the neutrons have the most abundance among the particles inside the HNS core. The neutron fraction, which is almost independent of baryonic density in the pure baryonic phase, becomes clearly smaller with rising baryonic density in the mixed phase. In contrast to the neutron fraction, the change of the proton fraction is insignificant at the mixed-phase region. The emergence of the mixed phase leads to the deleptonization of HNS matter due to the charge neutrality condition, while the quark fractions increase rapidly with the baryonic density. It can be generally concluded that the allowed baryonic density range of the mixed-phase core is reduced as a stiffer hybrid EOS is adopted.

To probe comparatively the outcomes of using the nonlocal extension of the NJL model, we display in Fig. 11 the hybrid EOSs derived by the LNJL model of RKH (HK). As well understood from this figure, the vector interaction in the LNJL model has a weaker influence on stiffening the quark EOS than the one in the NNJL model. In contrast to the NNJL approach, the width of the mixed phase in the LNJL scenario becomes larger with increasing η_V . It is worth noting that the NNJL model predicts the larger values of the critical surface tension $\tilde{\sigma}_c$ for a $2M_\odot$ HNS than the LNJL model (see Tables II and III), as the mixed phase is described by the Maxwell construction for $\sigma > \tilde{\sigma}_c$.

Incorporating the NICER measurements of J0030 + 0451 [29,30] and the constraint extracted from the most massive pulsar J0740 + 6620 [25], we show in Fig. 12 the mass-radius (M - R) profiles obtained by the different hybrid EOSs using both the NNJL and LNJL models. It can be

TABLE III. Same as Table II but for the quark interactions of RKH and HK given by the LNJL model.

| EOS | η_v | ρ_c (fm^{-3}) | e_c (GeVfm^{-3}) | P_c (MeVfm^{-3}) | M_{max} (M_{\odot}) | R (km) | $\frac{M_{(MP)}}{M_{\text{max}}}$ | Λ | $\tilde{\sigma}_c$ (MeVfm^{-2}) |
|------------|----------|----------------------------------|----------------------------------|----------------------------------|-------------------------------------|------------------|-----------------------------------|------------------|---|
| TF[90]-RKH | 0 | 1.03 [0.76–1.31] | 1.25 [0.85–1.66] | 278.221 [262.67] | 1.95 [1.98] | 11.37 [11.42] | 0.11 [0] | 23.57 [22.50] | 38.31 |
| | 0.22 | 1.10 [0.89–1.46] | 1.40 [1.05–2.00] | 420.37 [410.23] | 2.07 [2.08] | 11.02 [11.03] | 0.06 [0] | 11.02 [10.70] | 37.73 |
| | 0.44 | 1.13 [1.02–1.60] | 1.48 [1.30–2.36] | 607.25 [611.78] | 2.12 [2.12] | 10.65 [10.63] | 0.02 [0] | 6.25 [6.21] | 33.06 |
| TF[96]-RKH | 0 | 1.15 [0.88–1.50] | 1.41 [1.01–1.95] | 342.65 [326.07] | 1.88 [1.90] | 10.81 [10.85] | 0.12 [0] | 20.20 [19.05] | 49.62 |
| | 0.22 | 1.21 [1.05–1.67] | 1.55 [1.28–2.36] | 531.15 [528.45] | 1.97 [1.98] | 10.40 [10.39] | 0.05 [0] | 9.30 [8.91] | 47.57 |
| | 0.44 | 1.25 [1.23–1.86] | 1.65 [1.61–2.87] | 773.75 [819.10] | 2.01 [2.01] | 10.01 [9.95] | 0.01 [0] | 5.41 [5.02] | 41.06 |
| TF[90]-HK | 0 | 1.05 [0.74–1.13] | 1.27 [0.82–1.39] | 263.36 [243.88] | 1.94 [1.96] | 11.41 [11.48] | 0.13 [0] | 26.11 [25.75] | 29.17 |
| | 0.22 | 1.08 [0.86–1.37] | 1.38 [1.01–1.83] | 393.66 [380.71] | 2.06 [2.07] | 11.08 [11.10] | 0.07 [0] | 12.30 [12.02] | 34.53 |
| | 0.44 | 1.12 [0.99–1.52] | 1.47 [1.23–2.20] | 559.31 [557.45] | 2.11 [2.12] | 10.73 [10.73] | 0.03 [0] | 7.04 [6.87] | 32.13 |
| TF[96]-HK | 0 | 1.14 [0.86–1.38] | 1.40 [0.99–1.77] | 331.70 [311.86] | 1.87 [1.89] | 10.84 [10.89] | 0.13 [0] | 21.39 [20.57] | 43.65 |
| | 0.22 | 1.20 [1.02–1.60] | 1.54 [1.24–2.22] | 502.48 [495.00] | 1.97 [1.98] | 10.46 [10.46] | 0.06 [0] | 10.16 [9.80] | 45.14 |
| | 0.44 | 1.24 [1.19–1.79] | 1.64 [1.53–2.69] | 721.17 [747.95] | 2.00 [2.01] | 10.08 [10.04] | 0.02 [0] | 5.96 [5.61] | 40.84 |

concluded that the quark vector interaction is substantial in describing the HNS structure, because a large enough vector coupling strength η_v fulfills the $2M_{\odot}$ constraint. In each M - R relation, as the gravitational mass becomes larger, the onset of the baryon-quark stellar core reduces the star radius, and therefore, increases the compactness $\mathcal{C} = M/R$. Note that our findings are consistent with the observational constraints, showing that PSR J0030 + 0451, and PSR J0740 + 6620 could be described as an NS and an HNS without a pure quark core, respectively. On the other hand, a stable NS can be constituted with the maximum mass $M_{\text{max}} = 2.13$ (2.01) M_{\odot} for TF[90] (TF[96]). In this work, the possibility that the secondary object of GW190814 [59] is a massive HNS (NS) cannot be provided. For the sake of completeness, Tables II and III yield quantitatively the maximum mass configuration properties obtained using the NNJL and LNJL models, respectively. As reported, the maximum masses in the Maxwell construction are slightly larger than those in the Gibbs construction. In conclusion, our results exclude the formation of a stable HNS within the Maxwell construction due to not predicting the emergence of the pure quark phase in the star core, while in Ref. [9], on the contrary, the Maxwell construction can lead to the appearance of the pure quark core when

baryonic matter is treated in a RMF approximation and quark matter is similarly modeled by both the NNJL and LNJL models.

The tidal effects detected by the emission of the gravitational wave during the inspiral of a binary NS system at early stages impose strong constraints on the EOS of dense matter. The relation between the tidal distortion in a binary NS system and the EOS describing the NS structure is characterized by a single dimensionless parameter known as tidal deformability (polarizability) Λ , which is related to the tidal Love number k_2 and the star compactness $\mathcal{C} = M/R$ [60,61] as ($G = c = 1$):

$$\Lambda = \frac{2}{3}k_2\mathcal{C}^{-5}, \quad (47)$$

with

$$k_2 = \frac{8\mathcal{C}^5}{5}(1 - 2\mathcal{C})^2[2 + 2\mathcal{C}(y_R - 1) - y_R] \\ \times \{2\mathcal{C}[6 - 3y_R + 3\mathcal{C}(5y_R - 8)] \\ + 4\mathcal{C}^3[13 - 11y_R + \mathcal{C}(3y_R - 2) + 2\mathcal{C}^2(1 + y_R)] \\ + 3(1 - 2\mathcal{C})^2[2 - y_R + 2\mathcal{C}(y_R - 1)]\ln(1 - 2\mathcal{C})\}^{-1}. \quad (48)$$

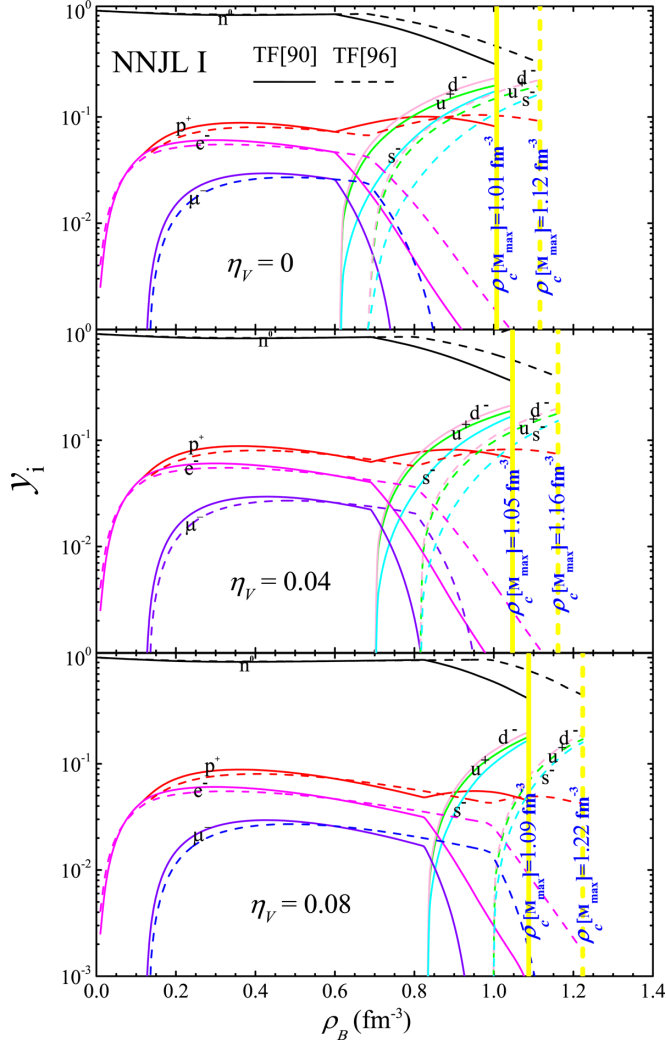


FIG. 9. Number fraction of baryons, leptons, and quarks as a function of baryonic density for the quark interaction of NNJL I at $\eta_V = 0$ (upper panel), $\eta_V = 0.04$ (middle panel), $\eta_V = 0.08$ (lower panel), combined with the baryonic interactions of TF[90] (solid lines) and TF[96] (dashed lines) via the Gibbs construction. The solid (dashed) vertical lines indicate the central baryonic densities of the maximum mass configurations obtained by the baryonic EOS of TF[90] (TF[96]).

In the above, y_R is obtained by the function $y(r)$ at the star radius R , satisfying the following nonlinear first-order differential equation, which can be solved simultaneously with the TOV Eqs. (45) and (46) at the boundary condition $y(0) = 2$ [62]:

$$r \frac{dy(r)}{dr} + y(r)^2 + F(r)y(r) + r^2 Q(r) = 0, \quad (49)$$

where

$$F(r) = \frac{1 - 4\pi r^2 [e(r) - P(r)]}{1 - \frac{2m(r)}{r}} \quad (50)$$

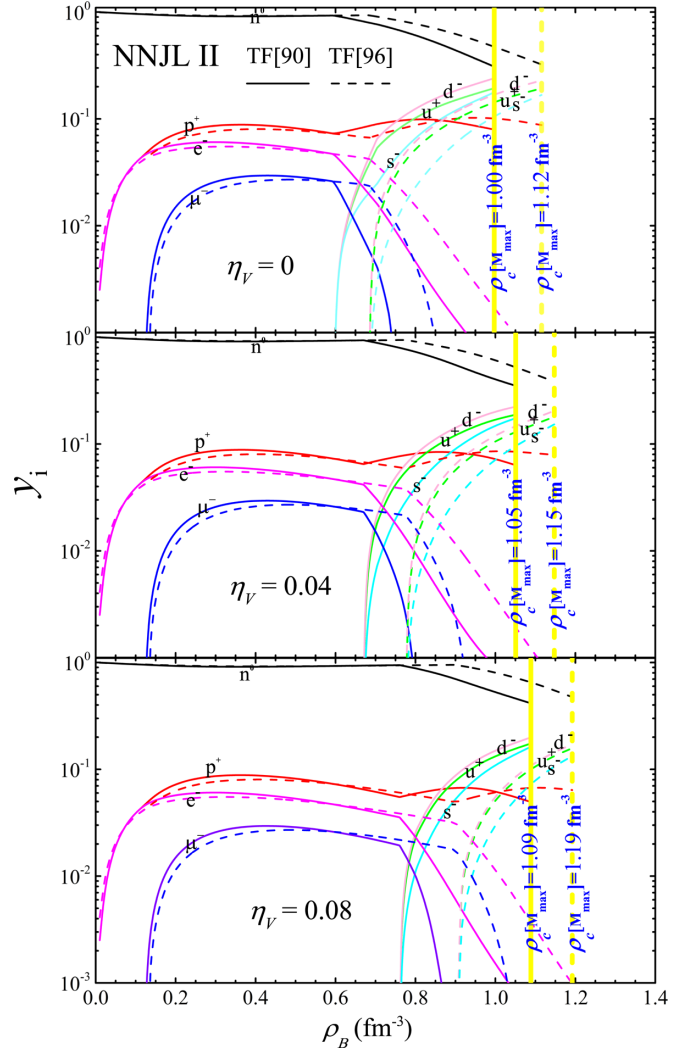


FIG. 10. Same as Fig. 9 but for the NNJL II interaction.

and

$$Q(r) = \frac{4\pi [5e(r) + 9P(r) + \frac{e(r)+P(r)}{dp/de} - \frac{6}{4\pi r^2}]}{1 - \frac{2m(r)}{r}} - \frac{4}{r^4} \left[\frac{m(r) + 4\pi r^3 P(r)}{1 - \frac{2m(r)}{r}} \right]^2. \quad (51)$$

With the historic detection of the GW170817 signal by the LIGO-Virgo scientific collaboration [26–28], more stringent constraints on the EOS of dense matter can be extracted. In Fig. 13, we display the tidal deformability Λ as a function of the gravitational mass (in units of the solar mass M_\odot). We also present in this figure the 90% confidence-level estimate $70 \leq \Lambda \leq 580$ for a $1.4M_\odot$, reported in Ref. [27]. Within the present approach, the core of a $1.4M_\odot$ NS is not dense enough to exceed the onset density for the emergence of the mixed phase. For a given baryonic EOS, the discrepancies between the tidal deformability of the hybrid EOSs, which appear only

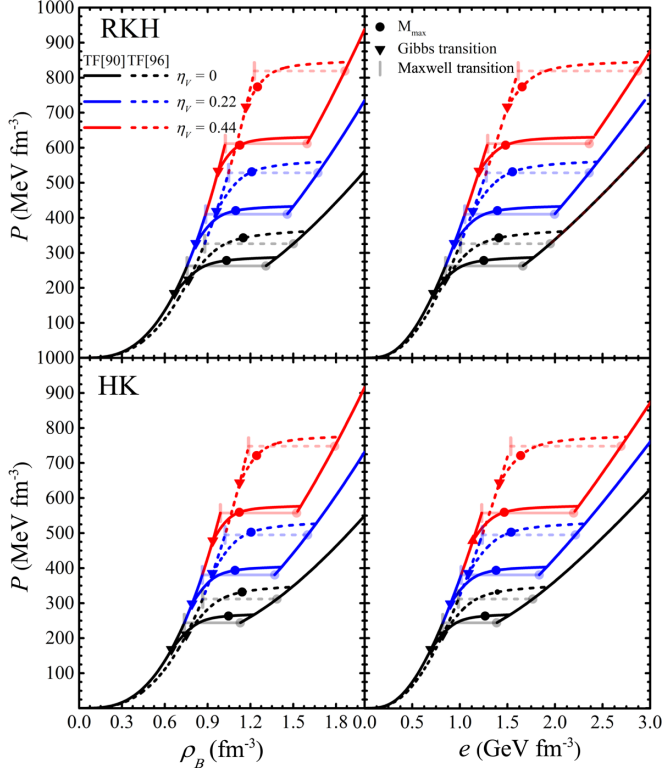


FIG. 11. Pressure as a function of baryonic density (left panels) and energy density (right panels) for the quark interactions of RKH (upper panels) and HK (lower panels) given by the LNJL model at $\eta_v = 0, 0.22, 0.44$, combined with the baryonic interactions of TF[90] (solid lines) and TF[96] (dashed lines) via the Gibbs construction, as the plateaus correspond to the Maxwell construction. The circles indicate the maximum mass configurations, as the EOS above the respective baryonic densities and energy densities is excluded. The onset of the baryon-quark phase transition in the star center is shown with the triangles and vertical slashes corresponding to the Gibbs and Maxwell constructions, respectively.

in the coexisting branches, are rather small. In general, by strengthening the repulsive effects in the quark (baryonic) EOS, the tidal deformability of an HNS can coincide with the lower (larger) values, as understood from the values reported in Tables II and III for the maximum mass configuration properties described by the NNJL and LNJL models, respectively. It is shown in these tables that the Maxwell construction predicts a slightly lower value of the tidal deformability for the maximum mass configuration than the Gibbs construction.

IV. SUMMARY AND CONCLUSION

In this work, we have studied the EOS of HNS matter for deep understanding about the structure of HNSs, employing a

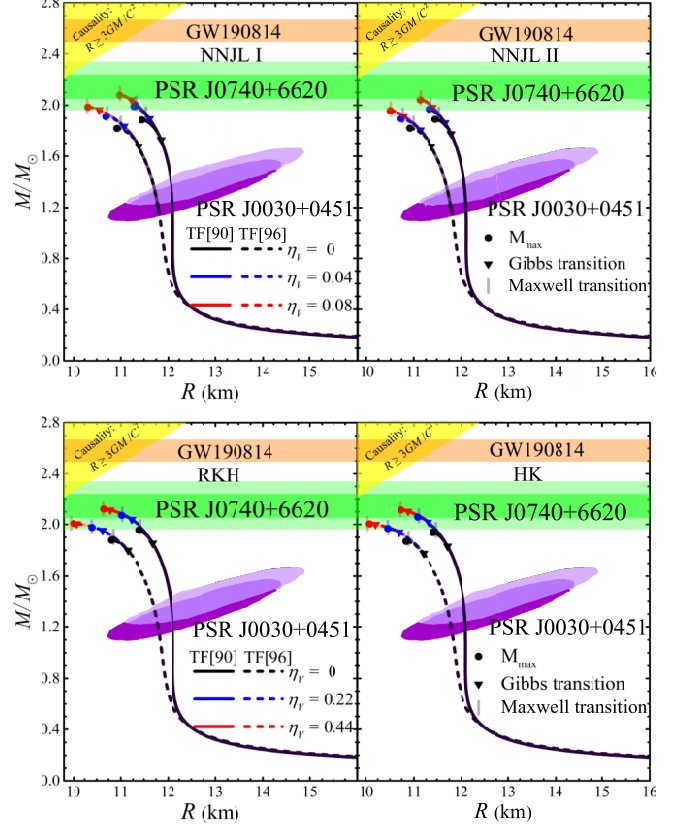


FIG. 12. Mass-radius diagrams for the quark interactions of NNJL I (upper left panel) and NNJL II (upper right panel) at $\eta_v = 0, 0.04, 0.08$, together with the quark interactions of RKH (lower left panel) and HK (lower right panel) given by the LNJL model at $\eta_v = 0, 0.22, 0.44$, combined with the baryonic interactions of TF[90] (solid lines) and TF[96] (dashed lines) via the Gibbs and Maxwell constructions. The circles and triangles (vertical slashes) indicate the maximum mass configurations, and onsets of the baryon-quark phase transition in the star center within the Gibbs (Maxwell) construction, respectively. The horizontal bands show the observational mass constraint from PSR J0740 + 6620 [25] and the gravitational mass inferred for the lighter component of GW190814 [59]. The areas of the mass-radius limits inferred from the NICER measurements of PSR J0030 + 0451 [29,30] are also shown. The region on the top left of each panel is excluded by causality [63].

semiclassical MF baryonic model based on the TF approximation and a nonlocal extension of the SU(3) NJL quark model to determine the deconfinement phase transition under the Gibbs and Maxwell constructions. Furthermore, we have carried out a comparison with the hybrid EOSs using the LNJL model for quark matter. Our results reflect a high-pressure nature for the baryon-quark mixed phase. The stiffness of the NNJL EOS turns out to be more significantly affected by the repulsive vector coupling strength η_v than the one

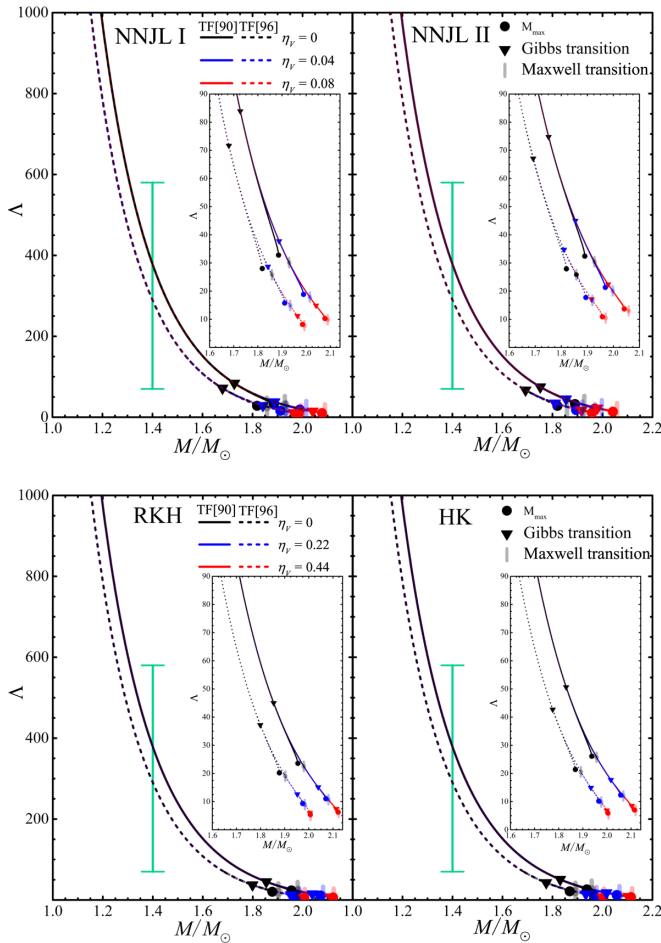


FIG. 13. Tidal deformability of HNSs as a function of gravitational mass (in units of the solar mass M_\odot) for the quark interactions of NNJL I (upper left panel) and NNJL II (upper right panel) at $\eta_v = 0, 0.04, 0.08$, together with the quark interactions of RKH (lower left panel) and HK (lower right panel) given by the LNjL model at $\eta_v = 0, 0.22, 0.44$, combined with the baryonic interactions of TF[90] (solid lines) and TF[96] (dashed lines) via the Gibbs and Maxwell constructions. The circles and triangles (vertical slashes) indicate the maximum mass configurations and onsets of the baryon-quark phase transition in the star center within the Gibbs (Maxwell) construction, respectively. The vertical bar shows the tidal deformability range of a $1.4M_\odot$ NS, obtained by the analysis of the GW170817 signal [27].

of the LNjL EOS. Hence, increasing η_v changes appreciably the mixed-phase characteristics, pushing the transition density and pressure to the higher values, while (contrary to what happens in the LNjL model) the coexistence width is reduced. Within the Gibbs construction, as predicted by the stiffer hybrid EOSs using the NNjL (LNjL) model, the center of a stable $2M_\odot$ HNS is not dense enough to lie into the pure quark phase, while the limit for the mass fraction of the mixed-phase core is estimated to be $\approx 12\%$ (7%), indicating that the dominant contribution to the gravitational mass comes from the pure baryonic phase. To describe a $2M_\odot$ HNS within the Maxwell construction, the critical surface tension, above which the Maxwell construction is favorable, is found to be larger for the hybrid EOSs using the NNjL model than the ones using the LNjL model, although the Maxwell construction leads to an unstable HNS due to not supporting the appearance of a pure quark core. According to the maximum mass configuration properties, stiffening the quark EOS, has an almost small influence on the tidal deformability of an HNS, as it can reach the lower values. Within this research, we cannot predict the possibility that the secondary component of GW190814 [59] is a massive HNS (NS). On the other hand, within the constraints from the analysis of the GW170817 event, the emergence of the mixed phase in the core region of a $1.4M_\odot$ NS is ruled out. In the future, we plan to extend this approach to provide deeper insight into the structure and composition of HNSs.

ACKNOWLEDGMENTS

The authors would like to thank University of Kashan for supporting this project under Grant No. 1073159/1 provided by the Research Council.

- [1] S. L. Shapiro and S. A. Teukolsky, *Black Holes, White Dwarfs, and Neutron Stars* (John Wiley and Sons, New York, 2008).
- [2] F. Weber, *Prog. Part. Nucl. Phys.* **54**, 193 (2005).
- [3] D. Blaschke, T. Klähn, and F. Sandin, *J. Phys. G* **35**, 014051 (2007).
- [4] F. Yang and H. Shen, *Phys. Rev. C* **77**, 025801 (2008).
- [5] O. Benhar and A. Cipollone, *Astron. Astrophys.* **525**, L1 (2011).
- [6] L. Bonanno and A. Sedrakian, *Astron. Astrophys.* **539**, A16 (2012).
- [7] D. Logoteta and I. Bombaci, *Phys. Rev. D* **88**, 063001 (2013).
- [8] S. Benić, D. Blaschke, D. E. Alvarez-Castillo, T. Fischer, and S. Typel, *Astron. Astrophys.* **577**, A40 (2015).
- [9] I. F. Ranea-Sandoval, S. Han, M. G. Orsaria, G. A. Contrera, F. Weber, and M. G. Alford, *Phys. Rev. C* **93**, 045812 (2016).
- [10] G. Baym, T. Hatsuda, T. Kojo, P. D. Powell, Y. Song, and T. Takatsuka, *Rep. Prog. Phys.* **81**, 056902 (2018).
- [11] K. Maslov, N. Yasutake, D. Blaschke, A. Ayriyan, H. Grigorian, T. Maruyama, T. Tatsumi, and D. N. Voskresensky, *Phys. Rev. C* **100**, 025802 (2019).
- [12] M. Ferreira, R. C. Pereira, and C. Providência, *Phys. Rev. D* **101**, 123030 (2020).
- [13] C.-J. Xia, T. Maruyama, N. Yasutake, T. Tatsumi, H. Shen, and H. Togashi, *Phys. Rev. D* **102**, 023031 (2020).
- [14] M. Maserà, L. Riccati, and E. Vercellin, Quark matter-99 proceedings, *Nucl. Phys. A* **661**, 1 (1999).

- [15] B. Friman, C. Höhne, J. Knoll, S. Leupold, J. Randrup, R. Rapp, and P. Senger, *The CBM Physics Book: Compressed Baryonic Matter in Laboratory Experiments*, Lecture Notes in Physics, Vol. 814 (Springer-Verlag, Berlin Heidelberg, 2011).
- [16] Y. Nambu and G. Jona-Lasinio, *Phys. Rev.* **122**, 345 (1961); **124**, 246 (1961).
- [17] M. Buballa, *Phys. Rep.* **407**, 205 (2005).
- [18] F. Marquez, A. Ahmad, M. Buballa, and A. Raya, *Phys. Lett. B* **747**, 529 (2015).
- [19] G. A. Contrera, D. G. Dumm, and N. N. Scoccola, *Phys. Lett. B* **661**, 113 (2008).
- [20] G. A. Contrera, D. Gomez Dumm, and N. N. Scoccola, *Phys. Rev. D* **81**, 054005 (2010).
- [21] K. Kashiwa, T. Hell, and W. Weise, *Phys. Rev. D* **84**, 056010 (2011).
- [22] P. Demorest, T. Pennucci, S. Ransom, M. Roberts, and J. Hessels, *Nature (London)* **467**, 1081 (2010).
- [23] E. Fonseca, T. T. Pennucci, J. A. Ellis, I. H. Stairs, D. J. Nice, S. M. Ransom, P. B. Demorest, Z. Arzoumanian, K. Crowter, T. Dolch *et al.*, *Astrophys. J.* **832**, 167 (2016).
- [24] J. Antoniadis, P. C. C. Freire, N. Wex, T. M. Tauris, R. S. Lynch, M. H. van Kerkwijk, M. Kramer, C. Bassa, V. S. Dhillon, T. Driebe *et al.*, *Science* **340**, 1233232 (2013).
- [25] H. T. Cromartie, E. Fonseca, S. M. Ransom, P. B. Demorest, Z. Arzoumanian, H. Blumer, P. R. Brook, M. E. DeCesar, T. Dolch, J. A. Ellis *et al.*, *Nat. Astron.* **4**, 72 (2020).
- [26] B. P. Abbott, R. Abbott, T. D. Abbott, F. Acernese, K. Ackley, C. Adams, T. Adams, P. Addesso, R. X. Adhikari, V. B. Adya *et al.*, *Phys. Rev. Lett.* **119**, 161101 (2017).
- [27] B. P. Abbott, R. Abbott, T. D. Abbott, F. Acernese, K. Ackley, C. Adams, T. Adams, P. Addesso, R. X. Adhikari, V. B. Adya *et al.*, *Phys. Rev. Lett.* **121**, 161101 (2018).
- [28] B. P. Abbott, R. Abbott, T. D. Abbott, F. Acernese, K. Ackley, C. Adams, T. Adams, P. Addesso, R. X. Adhikari, V. B. Adya *et al.*, *Phys. Rev. X* **9**, 011001 (2019).
- [29] T. E. Riley, A. L. Watts, S. Bogdanov, P. S. Ray, R. M. Ludlam, S. Guillot, Z. Arzoumanian, C. L. Baker, A. V. Bilous, D. Chakrabarty *et al.*, *Astrophys. J. Lett.* **887**, L21 (2019).
- [30] M. C. Miller, F. K. Lamb, A. J. Dittmann, S. Bogdanov, Z. Arzoumanian, K. C. Gendreau, S. Guillot, A. K. Harding, W. C. G. Ho, J. M. Lattimer *et al.*, *Astrophys. J. Lett.* **887**, L24 (2019).
- [31] M. Ghazanfari Mojarrad and J. Ranjbar, *Phys. Rev. C* **100**, 015804 (2019).
- [32] M. Ghazanfari Mojarrad and J. Ranjbar, *Ann. Phys. (NY)* **412**, 168048 (2020).
- [33] D. B. Blaschke, D. Gomez Dumm, A. G. Grunfeld, T. Klähn, and N. N. Scoccola, *Phys. Rev. C* **75**, 065804 (2007).
- [34] M. Orsaria, H. Rodrigues, F. Weber, and G. A. Contrera, *Phys. Rev. D* **87**, 023001 (2013).
- [35] M. Orsaria, H. Rodrigues, F. Weber, and G. A. Contrera, *Phys. Rev. C* **89**, 015806 (2014).
- [36] S. M. de Carvalho, R. Negreiros, M. Orsaria, G. A. Contrera, F. Weber, and W. Spinella, *Phys. Rev. C* **92**, 035810 (2015).
- [37] I. F. Ranea-Sandoval, M. G. Orsaria, G. Malfatti, D. Curin, M. Mariani, G. A. Contrera, and O. M. Guilera, *Symmetry* **11**, 425 (2019).
- [38] M. Brack and R. K. Bhaduri, *Semiclassical Physics* (Addison-Wesley, New York, 1997).
- [39] W. D. Myers and W. J. Swiatecki, *Ann. Phys. (NY)* **204**, 401 (1990).
- [40] W. D. Myers and W. J. Swiatecki, *Nucl. Phys. A* **601**, 141 (1996).
- [41] J. Randrup and E. Lima Medeiros, *Nucl. Phys. A* **529**, 115 (1991).
- [42] H. R. Moshfegh and M. Ghazanfari Mojarrad, *J. Phys. G* **38**, 085102 (2011).
- [43] M. Ghazanfari Mojarrad and S. K. Mousavi Khoroshtomi, *Int. J. Mod. Phys. E* **26**, 1750038 (2017).
- [44] H. R. Moshfegh and M. Ghazanfari Mojarrad, *Eur. Phys. J. A* **49**, 1 (2013).
- [45] M. Ghazanfari Mojarrad and R. Arabsaeidi, *Int. J. Mod. Phys. E* **25**, 1650102 (2016).
- [46] M. Ghazanfari Mojarrad, N. S. Razavi, and S. Vaezzade, *Nucl. Phys. A* **980**, 51 (2018).
- [47] M. Ghazanfari Mojarrad and N. S. Razavi, *Nucl. Phys. A* **986**, 133 (2019).
- [48] M. Brack, C. Guet, and H. B. Hakansson, *Phys. Rep.* **123**, 275 (1985).
- [49] G. Malfatti, M. G. Orsaria, G. A. Contrera, F. Weber, and I. F. Ranea-Sandoval, *Phys. Rev. C* **100**, 015803 (2019).
- [50] C. Sasaki, B. Friman, and K. Redlich, *Phys. Rev. D* **75**, 054026 (2007).
- [51] P. Rehberg, S. P. Klevansky, and J. Hüfner, *Phys. Rev. C* **53**, 410 (1996).
- [52] T. Hatsuda and T. Kunihiro, *Phys. Rep.* **247**, 221 (1994).
- [53] D. Voskresensky, M. Yasuhira, and T. Tatsumi, *Nucl. Phys. A* **723**, 291 (2003).
- [54] P. Danielewicz, R. Lacey, and W. G. Lynch, *Science* **298**, 1592 (2002).
- [55] R. C. Tolman, *Phys. Rev.* **55**, 364 (1939).
- [56] J. R. Oppenheimer and G. M. Volkoff, *Phys. Rev.* **55**, 374 (1939).
- [57] J. W. Negele and D. Vautherin, *Nucl. Phys. A* **178**, 123 (1973).
- [58] G. Baym, C. Pethick, and D. Sutherland, *Astrophys. J.* **170**, 299 (1971).
- [59] R. Abbott *et al.*, *Astrophys. J. Lett.* **896**, L44 (2020).
- [60] T. Hinderer, *Astrophys. J.* **677**, 1216 (2008).
- [61] T. Hinderer, B. D. Lackey, R. N. Lang, and J. S. Read, *Phys. Rev. D* **81**, 123016 (2010).
- [62] S. Postnikov, M. Prakash, and J. M. Lattimer, *Phys. Rev. D* **82**, 024016 (2010).
- [63] J. M. Lattimer and M. Prakash, *Science* **304**, 536 (2004).

Correction: The previously published Figure 12 contained a proof layout error with top and bottom panels switched and has been set right.